

Dark Matter Search Results from the Commissioning Run of PandaX-II

Andi Tan,² Xiang Xiao,¹ Xiangyi Cui,¹ Xun Chen,¹ Yunhua Chen,³ Deqing Fang,⁴ Changbo Fu,¹ Karl Giboni,¹ Franco Giuliani,^{1,5} Haowei Gong,¹ Shouyang Hu,⁶ Xingtao Huang,⁷ Xiangdong Ji,^{1,5,2,*} Yonglin Ju,⁸ Siao Lei,¹ Shaoli Li,¹ Xiaomei Li,⁶ Xinglong Li,⁶ Hao Liang,⁶ Qing Lin,^{1,†} Huaxuan Liu,⁸ Jianglai Liu,^{1,‡} Wolfgang Lorenzon,⁹ Yugang Ma,⁴ Yajun Mao,¹⁰ Kaixuan Ni,^{1,§} Kirill Pushkin,^{1,9} Xiangxiang Ren,¹ Michael Schubnell,⁹ Manbin Shen,³ Fang Shi,¹ Scott Stephenson,⁹ Hongwei Wang,⁴ Jiming Wang,³ Meng Wang,⁷ Qihong Wang,⁴ Siguang Wang,¹⁰ Xuming Wang,¹ Zhou Wang,⁸ Shiyong Wu,³ Mengjiao Xiao,¹ Pengwei Xie,^{1,¶} Binbin Yan,⁷ Yong Yang,¹ Jianfeng Yue,³ Xionghui Zeng,³ Hongguang Zhang,¹ Hua Zhang,⁸ Huanqiao Zhang,⁶ Tao Zhang,¹ Li Zhao,¹ Jing Zhou,⁶ and Xiaopeng Zhou¹⁰

(PandaX-II Collaboration)

¹*INPAC and Department of Physics and Astronomy, Shanghai Jiao Tong University, Shanghai Laboratory for Particle Physics and Cosmology, Shanghai 200240, China*

²*Department of Physics, University of Maryland, College Park, Maryland 20742, USA*

³*Yalong River Hydropower Development Company, Ltd., 288 Shuanglin Road, Chengdu 610051, China*

⁴*Shanghai Institute of Applied Physics, Chinese Academy of Sciences, 201800, Shanghai, China*

⁵*Center of High Energy Physics, Peking University, Beijing 100871, China*

⁶*China Institute of Atomic Energy, Beijing 102413, China*

⁷*School of Physics and Key Laboratory of Particle Physics and Particle Irradiation (MOE), Shandong University, Jinan 250100, China*

⁸*School of Mechanical Engineering, Shanghai Jiao Tong University, Shanghai 200240, China*

⁹*Department of Physics, University of Michigan, Ann Arbor, MI, 48109, USA*

¹⁰*School of Physics, Peking University, Beijing 100871, China*

(Dated: February 23, 2016)

We present the results of a search for WIMPs from the commissioning run of the PandaX-II experiment located at the China Jinping underground Laboratory. A WIMP search data set with an exposure of 306×19.1 kg-day was taken, while its dominant ^{85}Kr background was used as the electron recoil calibration. No WIMP candidates are identified, and a 90% upper limit is set on the spin-independent elastic WIMP-nucleon cross section with a lowest excluded cross section of $2.97 \times 10^{-45} \text{ cm}^2$ at a WIMP mass of $44.7 \text{ GeV}/c^2$.

I. INTRODUCTION

The particle physics nature of dark matter is one of most fundamental scientific questions. The leading candidates, weakly interacting massive particles (WIMPs), can be directly detected by looking for WIMP-nucleon scattering events in deep underground laboratories. In recent years, experiments using the so-called dual-phase xenon techniques have been continuously pushing the exclusion limits of the elastic WIMP-nucleon scattering cross section [1–5], into the parameter space predicted by various theoretical models [6].

The PandaX experiment located at China Jinping underground Lab (CJPL) [7] is a dual-phase xenon direct dark matter detection experiment [8]. The first phase of the experiment, PandaX-I, with a 120-kg sensitive liquid xenon (LXe) target, performed the WIMP search in 2014

with a 54×80.1 kg-day exposure, producing a strong limit on the WIMP-nucleon cross section for a WIMP mass of less than $10 \text{ GeV}/c^2$ [9, 10], strongly disfavoring all positive claims from other experiments [11–14]. The construction and installation of the second stage of the PandaX experiment, PandaX-II, with a half-ton scale LXe target, commenced after PandaX-I. In 2015, a series of engineering runs were carried out to test the new detector system. This is the largest running dual-phase xenon detector to-date. A brief physics commissioning run was taken from Nov. 21 to Dec. 14, 2015, without dedicated electron recoil calibration and with a strong ^{85}Kr background, based on which we report a WIMP search with a 306×19.1 kg-day exposure.

II. THE PANDAX-II EXPERIMENT

PandaX-II reuses most of the infrastructures of PandaX-I. The most significant upgrades are the new inner vessel constructed from stainless steel with much lower radioactivity, reducing the ^{60}Co activity by more than an order of magnitude, and a much larger xenon Time Projection Chamber (TPC). The cylindrical TPC, as shown in Fig. 1, contains 580 kg LXe in the sensitive

* Spokesperson: xdji@sjtu.edu.cn

† Now at Department of Physics, Columbia University

‡ Corresponding author: jianglai.liu@sjtu.edu.cn

§ Now at Department of Physics, University of California, San Diego

¶ Corresponding author: willandy@sjtu.edu.cn

volume enclosed by polytetrafluoroethylene (PTFE) reflective panels with an inner diameter of 646 mm and a maximum drift length of 600 mm. The drift field is defined by a cathode mesh (200- μm wire diameter with 5-mm pitch) placed at the bottom of the TPC and gate grid (100- μm wire diameter with 5-mm pitch) 5.5 mm below the liquid level. The liquid level can be adjusted remotely via an overflow mechanism. The electron extraction field is produced between the gate grid and an anode mesh located 5.5 mm above the liquid level with the same construction as the cathode. During the commissioning run, a voltage of -29 kV and -4.95 kV was applied to the cathode and gate, respectively, and the anode was kept at ground, resulting in a drift field of 400 V/cm in LXe, and an extraction field of 6 kV/cm in the gaseous xenon. Right outside the side PTFE panels, 58 Cu shaping rings are mounted to guarantee the uniformity of the drift field. A skin LXe volume with a thickness of ~ 40 mm is confined between the inner PTFE and a layer of outer PTFE panels. Two identical arrays of photomultiplier tubes (PMTs) were placed above and below the TPC, respectively, each consisting of 55 Hamamatsu-R11410 3-inch PMTs, to detect scintillation photons in the sensitive volume. The top PMT array is placed 46 mm above the anode, and the bottom array is located 66 mm below the cathode. A screen grid (200- μm wire diameter with 5-mm pitch), set at ground, is placed 6 mm above the bottom PMT array to shield the cathode high-voltage. Two additional PMT arrays are located at same heights as the 3-in arrays, each with 24 Hamamatsu-R8520-406 1-inch PMTs, to produce veto signals in the skin volume. The PMT voltage divider for the 3-in PMTs uses a split positive and negative HV ($\sim \pm 650$ V) scheme to reduce the relative potential to the ground [15]. The average random PMT rates (“dark count rate”) for the R11410 PMTs were measured to be ~ 0.5 kHz, significantly improved from PandaX-I [16]. Same as that in PandaX-I, the signals from each PMT are amplified by a factor of 10, then get fed into the 100 MHz digitizer channels.

III. DATA PROCESSING AND SELECTION CUTS

The same data acquisition setup from PandaX-I is used for PandaX-II. Given the 60 cm depth of the TPC, the maximum time separation between the prompt photon signal in the liquid (S1) and the delayed proportional scintillation signal in the gas (S2) is estimated to be 350 μs . The length of each readout window is now 1 ms (200 μs in PandaX-I), with 500 μs before and after the trigger. The trigger is generated primarily on S2s for low energy events < 10 keV_{ee} electron equivalent energy [17] with a trigger threshold of 79 photoelectrons (PE), and higher energy events are mostly triggered by S1s.

The data processing and signal selection followed the same framework as in Ref. [10], converting information from the raw waveforms of individual PMTs into photo-

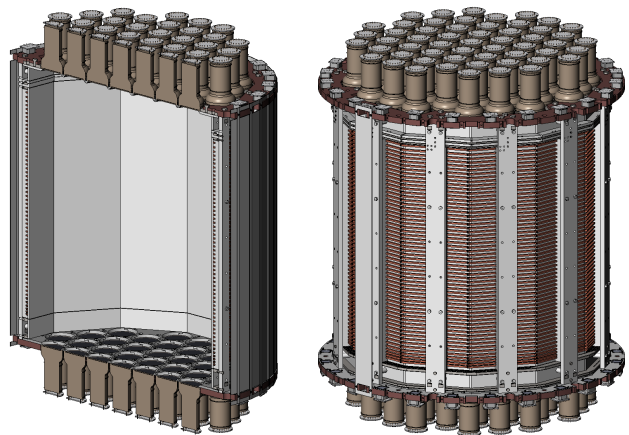


FIG. 1. Design drawings of PandaX-II TPC, left: cross-sectional view with both inner and outer PTFE panels, right: full view with skin volume exposed. See text for details.

electrons and timing for S1s and S2s, vertex position, etc. The baseline calculation was improved to correct drifts within one readout window. After the gain correction, a threshold of 0.25 PE in amplitude is used for finding PMT hits from each waveform. Clusters are formed for time correlated hits, with each cluster tagging into either a S1 signal, S2 signal, or noise, based on the shape of the summed waveform over all channels. The discrimination between S1 and S2 signals relies on the full-width-10%-maximum and the “roughness” of the waveform. At least three PMT hits are required for a valid S1 signal to suppress random coincidence among PMTs. Veto PMTs do not participate in the clustering, but a coincidence between the veto arrays and a S1 will veto the entire event. The threshold to generate a veto was estimated to be ~ 150 keV_{ee} in the skin region from a comparison between the data and Monte Carlo (MC) simulation.

On average the ratio of photoelectrons collected by the top and bottom PMT arrays is 1 : 2 for S1 and 2.2 : 1 for S2. To suppress random S1-like signals produced by the discharges on the electrodes or the so-called “gamma-X” events [18] in the charge-insensitive regions, both likely to happen close to the PMT arrays, selection cuts on the average photoelectrons per-fired-PMT as well as the ratio of max-to-total photoelectrons have been applied. Selection cuts are also set on the top-bottom ratio of S2 signals to remove spurious events located at the very edge and potential misidentified noises. In a given waveform, the maximum number of S1-like signals passing all quality cuts is limited to two, and the maximum one is chosen to pair with S2. To suppress events with incorrectly associated S1 and S2, the vertical location encoded by the top-bottom asymmetry in S1 is required to be consistent with that from the drift time. Finally, to avoid afterpulsing following an energetic event or discharge in the TPC, a > 10 ms separation between adjacent events is required in the dark matter data.

The horizontal vertex position is reconstructed based

on the charge pattern of S2 on the top PMT array. Like in PandaX-I, both a center-of-gravity and a template matching reconstruction methods are used and cross checked. The average difference between the two is 10.8 mm within the fiducial volume (FV, defined later). This is a measure of the reconstruction uncertainty, which leads to an uncertainty in the fiducial volume determination. The vertical position is obtained by the drift time, i.e. the time difference between S2 and S1, taking a drift speed of 1.7 mm/ μ s estimated from measured maximum drift time of 350 μ s, also consistent with Ref. [19] under a drift field of 400 V/cm.

IV. DETECTOR CALIBRATIONS

To calibrate the detector response, a neutron source (^{252}Cf) and two γ sources (^{60}Co and ^{137}Cs) were deployed through two PTFE tubes at different heights surrounding the inner vessel. Neutrons can excite xenon nuclei or produce metastable nuclear states, leading to de-exciting γ rays at 40 (^{129}Xe), 80 (^{131}Xe), 164 (^{131m}Xe), and 236 keV (^{129m}Xe). Photo-absorption γ peaks were used to calibrate the detector response. The 164 keV γ events were uniformly distributed in the detector and were used to produce a uniformity correction for the S1 and S2 signals. A 3-D correction map was produced for S1. For the S2 signals, the vertical uniformity correction was obtained by fitting S2 vs. the drift time using an exponential decay constant τ , known as the electron lifetime. As expected, τ improved over time due to continuous xenon purification from 240 μ s to 552 μ s with an average of 324 μ s during the entire run. The S2 distribution in the horizontal plane was used to produce a 2-D correction map, independent of the drift time.

The above uniformity correction was applied to all events. For each event, the electron equivalent energy E_{ee} can be reconstructed as

$$E_{ee} = W \times \left(\frac{S1}{\text{PDE}} + \frac{S2}{\text{EEE} \times \text{SEG}} \right), \quad (1)$$

in which $W = 13.7$ eV is the average work function to produce either an electron or photon [20]. PDE, the photon-detection efficiency, EEE, the electron extraction efficiency, and SEG, the single-electron gain in PE/e, are the three key detector parameters to be determined. To obtain SEG, the smallest S2 signals in the data were identified as the single electron signals. Their photoelectron distribution was fit with a Gaussian function, from which $\text{SEG} = 22.1 \pm 0.7$ with a resolution $\sigma = 7.41$ PE/e was obtained. To extract the other two parameters, the peak values of $S1/E_{ee}$ and $S2/E_{ee}$ are plotted for all γ peaks (Fig. 2), where the true energy of the γ s are taken as E_{ee} . A linear fit is then performed on the data points. The scattering of data points along the line indicates systematic effects such as the non-uniformity and nonlinearity in S1 and S2. The best fit values, $\text{PDE} = 11.7\%$, $\text{EEE} = 48.1\%$, were compared with those

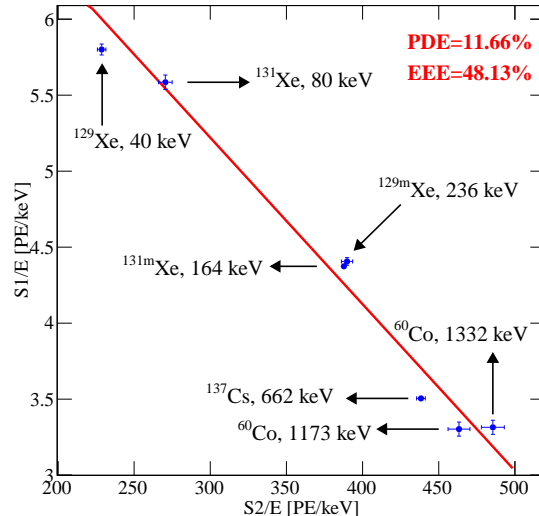


FIG. 2. Linear fit in $S2/E_{ee}$ vs. $S1/E_{ee}$ for all γ peaks. Each γ peak was fit with a 2-D Gaussian in the (S1, S2) plane with anti-correlation taken into account; only fit uncertainties are reflected on the data points.

obtained by taking the ratio of the observed peaks in S1 and S2 to the expected yield of photons and electrons from the NEST model [20]. The difference leads to a relative uncertainty of 5.6% in PDE and 7.1% in EEE.

The detector response to the low energy nuclear recoil (NR) events was calibrated using ^{252}Cf data. The $\log_{10}(S2/S1)$ vs. S1 of the NR events is shown in Fig. 3. In total, 547 NR events are identified for S1 between 3 to 45 PE in the FV. The MC predictions of the NR signal distribution were obtained from a combination of Geant4-based program and the NEST model with the extracted PDE, EEE, and SEG from calibration. In simulating photoelectrons, results from Ref. [21] were used to incorporate double photoelectron emissions from the 3-in PMTs. Vertical uniformity in S2 due to electron lifetime in the data and the S2 trigger threshold were also considered in the MC. The median value of the MC is compared to the data in Fig. 3. A much better agreement can be achieved by tuning the ratio of the initial number of excitation and ionization by a factor of 1.5 in NEST. The width of the NR band in the tuned MC also agrees with the data. Therefore, we adopted the tuned MC as the default model to predict the WIMP NR distributions. The NR efficiency was evaluated by a comparison between the data and MC on the event 2-D distribution in (S1, S2), leading to a parametrization

$$\epsilon = 0.94 \left[e^{-\frac{S1-6.21}{1.66}} + 1 \right]^{-1} \left[e^{-\frac{S2_{\text{raw}}-79.3}{20.8}} + 1 \right]^{-1}, \quad (2)$$

where $S2_{\text{raw}}$ is the raw S2 before the electron lifetime correction. The energy independent factor, 0.94, was obtained by choosing high energy NR events with $S1 > 20$ PE

and within $\pm 3\sigma$ of the NR band, and releasing the selection cuts.

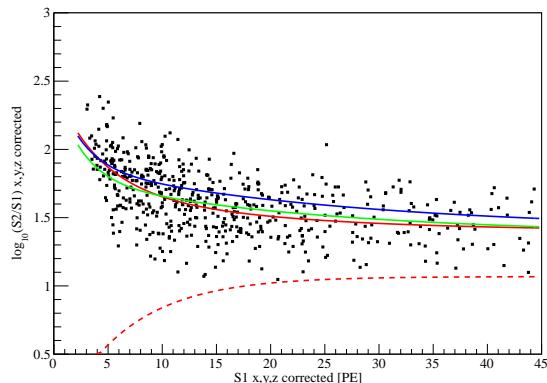


FIG. 3. The comparison of ^{252}Cf neutron calibration data with the median from the original NEST model (blue line) and the tuned model (green line). A fit to the median of the data is given by the red line. The dashed red line is the NR 99.99% acceptance line based on the tuned MC model.

In contrast, the NEST electron recoil (ER) model [22] appears to describe the low energy data in the γ calibration and WIMP search runs. However, inside the FV, the statistics of the low energy events in γ calibration runs were insufficient due to the self-shielding effect from LXe. We shall resort to the WIMP search data to model the ER distribution.

V. BACKGROUNDS

As in Ref. [10], the background is categorized into three components: the ER, neutron, and accidental background.

The ER background consists of external background due to radioactivities in the detector materials, and internal backgrounds due to krypton and radon. Before the detector assembly, the components were assayed with a high purity Germanium counting station at CJPL. The assay results, tuned to fit the data in high energy, were used as the input of the Geant4-based MC to calculate the external ER background at low energy. In the FV, such background is expected to be 0.21 mDRU (1 mDRU = 10^{-3} evts/keV/kg/day).

In our data, significant number of low energy ER events were found and they distributed uniformly in the detector. They were identified as ^{85}Kr β -decay events (half-life 10.72 y) with a 99.563% probability of single β emission and 0.434% $\beta - \gamma$ delayed-coincident emission. The krypton in xenon was likely introduced by an air leak during the previous fill and recuperation cycle. By fitting the low energy ER events in the dark matter search data, the ^{85}Kr is estimated to be 0.082 mBq/kg or 15.04 mDRU with 3% uncertainty. Assuming a concentration

of 2×10^{-11} in natural Kr, this leads to a Kr mole fraction of 437 ± 13 ppt in LXe, consistent with the offline gas sample measurement using the technique from Ref. [23]. The $\beta - \gamma$ analysis gave an independent estimate of 507 ± 46 ppt Kr concentration. The difference in the mean values from the two methods, or 17%, is taken as the systematics uncertainty of the krypton background.

The radon level in LXe can be evaluated by identifying $\beta - \alpha$ and $\alpha - \alpha$ coincidence events. ^{222}Rn was estimated by the ^{214}Bi - ^{214}Po events to be $6.57 \mu\text{Bq/kg}$ in the FV. ^{220}Rn was estimated by the ^{212}Bi - ^{212}Po and ^{220}Rn - ^{216}Po events to be 0.54 and 0.41 $\mu\text{Bq/kg}$ in the FV, respectively.

Using MC, the contributions of low energy background discussed above are summarized in Table I.

Item	Background (mDRU)
Total	15.33
^{85}Kr	15.04
^{222}Rn	0.075
^{220}Rn	0.021
PMT arrays & bases	0.097
PTFE wall	0.021
Inner vessel	0.045
Others IV components	0.026
Cu outer vessel	0.016

TABLE I. Summary of ER background from different components, including Rn, Kr, activated Xe, and other detector components. The uncertainty is dominated by the ^{85}Kr (17%) based on two different analysis methods.

The neutron background can also be produced by the radioactivities of the detector components. In our case, the PTFE material was measured to contain 3 mBq/kg ^{238}U , of which the (α ,n) neutrons dominate the neutron background rate. Using the SOURCES-4A code [24] with material radioactivities as inputs, the raw neutron rate and energy spectrum were determined. The neutron background was then calculated using the Geant4-NEST-based MC to be 0.06 events in the final data sets after all selection cuts, with a conservatively estimated uncertainty of 100%.

The accidental background is produced by random coincidence of S1-like and S2-like signals. To evaluate it, dark matter search data were used to search for isolated S1 and S2 signals. Since single small S1s are below the trigger threshold, they were searched in the $350 \mu\text{s}$ pre-trigger window of each event triggered by high energy S1. The rate was determined to be 2.8 ± 0.1 Hz within the S1 range cut. In the same data set, 28069 single S2 events were identified within the final S2 range cut and radius cut. When pairing the single S1 and S2 randomly in time, and with all coincidence selection cuts applied (which suppresses random events significantly), 0.70 qualified accidental events are expected to survive with a 25% uncertainty estimated from the variation of S1 rates during the run.

The final expected background budget including ER, accidental, and neutron background is summarized in Ta-

ble II.

	ER	Accidental	Neutron	Total Expected	Total observed
All	611	5.9	0.13	617 ± 104	728
Below NR median	2.5	0.7	0.06	3.2 ± 0.71	2

TABLE II. The expected background events in 19.1 live-day dark matter search data in the FV, before and after the NR median cut. The uncertainties of the total expected background in the table are obtained based on the 17%, 25%, and 100% uncertainties in the ER, accidental, and neutron background, respectively. Both the uncertainties from the ER rate (17%) and leakage fraction (50%) have been taken into account in that of the ER background below the NR median. See text for details. Number of events from the data are shown in the last column.

VI. FINAL CANDIDATES AND WIMP CROSS SECTION LIMIT

Only events with single S2 were selected into the final candidate set. The FV cut was determined to be within $r^2 < 60000 \text{ mm}^2$ and $20 \mu\text{s} < \text{drift time} < 346 \mu\text{s}$. The horizontal space facing the outermost ring of the 3-in PMTs is removed to avoid leakage from poorly reconstructed events, and the vertical cut is asymmetric since the bottom array has been shielded by 66 mm of LXe. The vertex distributions in the data and MC are consistently flat within the FV. The amount of LXe in the cut is estimated to be $306 \pm 20 \text{ kg}$ where the uncertainty arises from the 10.8 mm uncertainty in position reconstruction.

A cut-based analysis was used to select dark matter candidate only from the events below the NR median curve from the data and above the 99.99% NR acceptance curve from the NEST MC (shown in Fig. 3). To estimate the ER background leaking under the NR median curve (in the lack of dedicated ER calibration), we used the distribution of the dark matter search data in the $(\log_{10}(S2/S1), S1)$ plane above the 33.3%-NR-acceptance curve (1/3 of the NR events are located above it) for the NR events, performing Gaussian fits to the data. The Gaussian leakage fraction was estimated to be $0.4 \pm 0.2\%$ below the NR median curve, confirmed by repeating the same estimate but including also data below the 33.3%-NR-acceptance curve.

Based on the expected background, the final S1 range cut was chosen to be between 3 to 45 PE to give the optimal median sensitivity, corresponding to an average energy window between 1.3 to 8.7 keV_{ee}. S2s are required to be between 100 PE (raw) and 10000 PE (uniformity corrected).

The event rates after various selection cuts are summarized in Table III. After the FV cut, 728 events are selected. The vertex distribution of all events before and after the FV cut is shown in Fig. 4.

Cut	#Events	Rate (Hz)
All triggers	4779083	2.89
Single S2 cut	1833756	1.11
Quality cut	1262906	0.76
Skin veto cut	1081044	0.65
S1 range	45883	2.77×10^{-2}
S2 range	29755	1.80×10^{-2}
Fiducial volume	728	4.40×10^{-4}

TABLE III. The event rate in the dark matter runs after various analysis cuts.

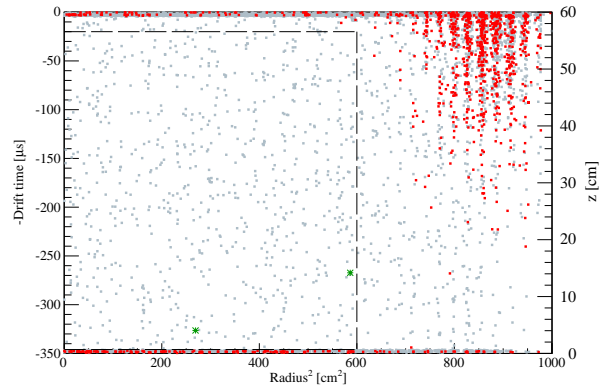


FIG. 4. Position distribution of events that pass all selection cuts (gray points), and those below the NR median (outside FV: red points; inside FV: green stars), with FV cuts indicated as the black dashed box. The red points clustered at the top, bottom and upper right corner correspond to edgy events losing electrons on the electrodes or PTFE wall, leading to a suppression of S2.

The $\log_{10}(S2/S1)$ vs. S1 distribution for the 728 candidates is shown in Fig. 5. Two events were found just below the NR median curve, with their vertices indicated in Fig. 4. Detailed examinations confirmed the high quality of these two events. The distribution of $\log_{10}(S2/S1)$ relative to the median of the data supports the Gaussian assumption in estimating the ER leakage fraction.

The final 90% upper limit for the spin-independent isoscalar WIMP-nucleon cross section was calculated based on the two events and 3.2 ± 0.71 expected background events (Table II) using the CLs method [25, 26] with the same standard assumptions as in Ref. [10]. The final results are shown in Fig. 6, with recent results from PandaX-I [10], XENON100 [3], LUX [5], SuperCDMS [27], and DarkSide [28] overlaid. Our upper limit lies within the $\pm 1\sigma$ sensitivity band, and is more constraining due to the downward fluctuation of the background. In comparison, the upper limit computed based on the original NEST prediction is weakened by about a factor of 2 in the high mass region but approaches a factor of 1.2 at low mass ($\sim 10 \text{ GeV}/c^2$). The lowest cross section limit obtained is $2.97 \times 10^{-45} \text{ cm}^2$ at a WIMP mass of 44.7 GeV/ c^2 , which represents an improvement of more

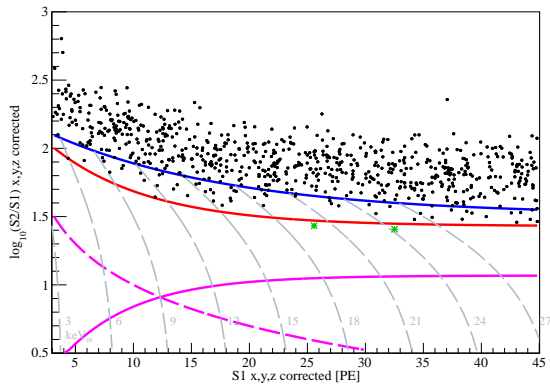


FIG. 5. The distribution of $\log_{10}(S2/S1)$ versus $S1$ for dark matter search data. The median of the NR calibration band is indicated as the red curve. The dashed magenta curve is the equivalent 100 PE cut on $S2$. The solid magenta and blue curves are the 99.99% and 33.3% NR acceptance curves, respectively. The grey dashed curves are the equal energy curves with NR energy indicated in the figures. The two data points located below the NR median curve are highlighted in green stars.

than a factor of three from PandaX-I, and even more in the low WIMP mass region. The major improvements include the exposure (a factor of ~ 1.35), the photon detection (PDE 11.7% vs. 9.6%), the $S2$ selection cut ($9.4 e$ vs $19.7 e$, although in PandaX-II a significant depth dependent efficiency variation is present due to the electron lifetime), the $S1$ window ($[3, 45]$ vs. $[2, 30]$ PE), and the expected background (3.2 vs. 6.9 events). The cross section limit at WIMP mass of 10, 100, and $300 \text{ GeV}/c^2$ are 8.43×10^{-44} , 4.34×10^{-45} , and $1.13 \times 10^{-44} \text{ cm}^2$, respectively. At low WIMP mass region down to $5 \text{ GeV}/c^2$, our exclusion limit is competitive with SuperCDMS [27]. At high WIMP mass region, our results are within a factor of ~ 1.5 to the final 225-day XENON100 results [3], although with only 19.1 days of live-time. However, our results do not quite scale with the LUX results (with a factor of 2.4 of exposure) [5] primarily due to the high krypton background.

VII. CONCLUSIONS AND OUTLOOK

In conclusion, we report the WIMP search results using the commissioning data of the PandaX-II experiment with an exposure of $306 \times 19.1 \text{ kg}\cdot\text{day}$. No dark matter candidates were identified above background and 90% upper limit is set on the spin-independent elastic WIMP-nucleon cross section with a lowest excluded value of

$2.97 \times 10^{-45} \text{ cm}^2$ at a WIMP mass of $44.7 \text{ GeV}/c^2$, a significant step-forward from PandaX-I. After a brief maintenance period to distill krypton from xenon, the experiment is expected to resume physics data taking in spring 2016, and soon to explore previously unattainable WIMP

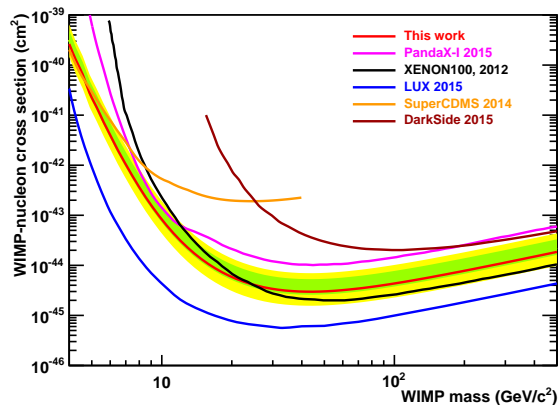


FIG. 6. The 90% C.L. upper limit for the spin-independent isoscalar WIMP-nucleon cross section from the PandaX-II commissioning run (red). A selected set of recent world results are plotted for comparison: PandaX-I final results [10] (magenta), XENON100 225 day results [3] (black), LUX 2015 results [5] (blue), SuperCDMS 2014 [27] (orange), and DarkSide 2015 [28] results (brown). The $\pm 1\sigma$ and 2σ sensitivity bands are shown in green and yellow, respectively.

parameter space.

ACKNOWLEDGMENTS

This project has been supported by a 985-III grant from Shanghai Jiao Tong University, grants from National Science Foundation of China (Nos. 11435008, 11455001, 11505112 and 11525522), and a grant from the Office of Science and Technology in Shanghai Municipal Government (No. 11DZ2260700). This work is supported in part by the Chinese Academy of Sciences Center for Excellence in Particle Physics (CCEPP). The project is also sponsored by Shandong University, Peking University, and the University of Maryland. We also would like to thank Dr. Xunhua Yuan and Chunfa Yao of China Iron & Steel Research Institute, and we are particularly indebted to Director De Yin from Taiyuan Iron & Steel (Group) Co. LTD for crucial help on nuclear-grade steel plates. Finally, we thank the following organizations and personnel for indispensable logistics and other supports: the CJPL administration including directors Jianping Cheng and Kejun Kang and manager Jianmin Li, and the Yalong River Hydropower Development Company Ltd.

[1] J. Angle *et al.* (XENON10), Phys. Rev. Lett. **107**, 051301 (2011), [Erratum: Phys. Rev. Lett.110,249901(2013)],

arXiv:1104.3088 [astro-ph.CO].

- [2] D. Yu. Akimov *et al.*, Phys. Lett. **B709**, 14 (2012), arXiv:1110.4769 [astro-ph.CO].
- [3] E. Aprile *et al.* (XENON100), Phys. Rev. Lett. **111**, 021301 (2013), arXiv:1301.6620 [astro-ph.CO].
- [4] D. S. Akerib *et al.* (LUX), Phys. Rev. Lett. **112**, 091303 (2014), arXiv:1310.8214 [astro-ph.CO].
- [5] D. S. Akerib *et al.* (LUX), (2015), arXiv:1512.03506 [astro-ph.CO].
- [6] P. Cushman *et al.*, in *Community Summer Study 2013: Snowmass on the Mississippi (CSS2013) Minneapolis, MN, USA, July 29-August 6, 2013* (2013) arXiv:1310.8327 [hep-ex].
- [7] Y.-C. Wu *et al.*, Chin. Phys. **C37**, 086001 (2013), arXiv:1305.0899 [physics.ins-det].
- [8] X. Cao *et al.* (PandaX), Sci. China Phys. Mech. Astron. **57**, 1476 (2014), arXiv:1405.2882 [physics.ins-det].
- [9] M. Xiao *et al.* (PandaX), Sci. China Phys. Mech. Astron. **57**, 2024 (2014), arXiv:1408.5114 [hep-ex].
- [10] X. Xiao *et al.* (PandaX), Phys. Rev. **D92**, 052004 (2015), arXiv:1505.00771 [hep-ex].
- [11] R. Bernabei *et al.* (DAMA), Eur. Phys. J. **C56**, 333 (2008), arXiv:0804.2741 [astro-ph].
- [12] C. E. Aalseth *et al.* (CoGeNT), Phys. Rev. Lett. **106**, 131301 (2011), arXiv:1002.4703 [astro-ph.CO].
- [13] G. Angloher *et al.*, Eur. Phys. J. **C72**, 1971 (2012), arXiv:1109.0702 [astro-ph.CO].
- [14] R. Agnese *et al.* (CDMS), Phys. Rev. Lett. **111**, 251301 (2013), arXiv:1304.4279 [hep-ex].
- [15] A. M. M. Elsieid, K. L. Giboni, and X. Ji, JINST **10**, T01003 (2015).
- [16] S. Li *et al.*, (2015), accepted by JINST, arXiv:1511.06223 [physics.ins-det].
- [17] X. Ren, X. Chen, X. Ji, S. Li, S. Lei, J. Liu, M. Wang, M. Xiao, P. Xie, and B. Yan, (2016), arXiv:1602.00858 [physics.ins-det].
- [18] J. Angle *et al.* (XENON), Phys. Rev. Lett. **100**, 021303 (2008), arXiv:0706.0039 [astro-ph].
- [19] K. Yoshino, U. Sowada, and W. F. Schmidt, Phys. Rev. **A14**, 438 (1976).
- [20] B. Lenardo, K. Kazkaz, M. Szydagis, and M. Tripathi, IEEE Trans. Nucl. Sci. **62**, 3387 (2015), arXiv:1412.4417 [astro-ph.IM].
- [21] C. H. Faham, V. M. Gehman, A. Currie, A. Dobi, P. Sorensen, and R. J. Gaitskell, JINST **10**, P09010 (2015), arXiv:1506.08748 [physics.ins-det].
- [22] From the spreadsheet at http://lux.physics.ucdavis.edu/~szydagis/NEST_LXe_LYandQYields_VsFieldParticle_Calc_Site.xlsx.
- [23] A. Dobi, C. G. Davis, C. Hall, T. Langford, S. Slutsky, and Y.-R. Yen, Nucl. Instrum. Meth. **A665**, 1 (2011), arXiv:1103.2714 [astro-ph.IM].
- [24] W. Wilson *et al.*, *SOURCES4A: A Code for Calculating (α , n), Spontaneous Fission, and Delayed Neutron Sources and Spectra*, Tech. Rep. LA-13639-MS (Los Alamos National Laboratory, 1999).
- [25] A. L. Read, J. Phys. **G28**, 2693 (2002).
- [26] T. Junk, Nucl. Instrum. Meth. **A434**, 435 (1999), arXiv:9902006 [hep-ex].
- [27] R. Agnese *et al.* (SuperCDMS), Phys. Rev. Lett. **112**, 241302 (2014), arXiv:1402.7137 [hep-ex].
- [28] P. Agnes *et al.* (DarkSide), (2015), arXiv:1510.00702 [astro-ph.CO].